Hydride-Containing Pt-doped Cu-rich Nanoclusters: Synthesis, Structure, and Electrocatalytic Hydrogen Evolution

Rhone P. Brocha Silalahi, Hao Liang, Yongsung Jo, Jian-Hong Liao, Tzu-Hao Chiu, Ying-Yann Wu, Xiaoping Wang, Samia Kahlal, Qi Wang, Woojun Choi, et al.

Hydride-Containing Pt-doped Cu-rich Nanoclusters: Synthesis, Structure, and Electrocatalytic Hydrogen Evolution

Rhone P. Brocha Silalahi,[a] Hao Liang,[b] Yongsung Jo,[c] Jian-Hong Liao,[a] Tzu-Hao Chiu,[a] Ying-Yann Wu,[a] Xiaoping Wang,[d] Samia Kahlal,[b] Qi Wang,[b] Woojun Choi,[c] Dongil Lee,*[c] Jean-Yves Saillard,*[b] and C. W. Liu*[a]

[a] Dr. R. P. B. Silalahi, Dr. J.-H. Liao, T.-H. Chiu, Dr. Y.-Y. Wu, Prof. Dr. C. W. Liu
Department of Chemistry
National Dong Hwa University
No. 1, Sec. 2, Da Hsueh Rd. Shoufeng, Hualien 97401 (Taiwan R. O. C.)
E-mail: chenwei@gms.ndhu.edu.tw
[b] H. Liang, Dr. Q. Wang, Dr. S. Kahlal, Prof. Dr. J.-Y. Saillard
Univ Rennes
CNRS, ISCR-UMR 6226, F-35000 Rennes, France
[c] Y. Jo, Dr. W. Choi, Prof. Dr. D. Lee
Department of Chemistry
Yonsei University
Seoul 03722, Republic of Korea
[d] Dr. X. Wang
Neutron Scattering Division
Neutron Sciences Directorate
Oak Ridge National Laboratory, Oak Ridge, Tennessee 37831, United States

Supporting information for this article is given via a link at the end of the document.

Abstract: A structurally precise hydride-containing Pt-doped Cu-rich nanocluster $[PtH_2Cu_{14}\{S_2P(O^iPr)_2\}_6(CCPh)_6]$ (**1**) has been synthesized. It consists of a bicapped icosahedral Cu_{14} cage that encapsulates a linear PtH_2 unit. Upon the addition of two equivalents of CF_3COOH to **1**, two hydrido clusters are isolated. These clusters are $[PtHCu_{11}\{S_2P(O^iPr)_2\}_6(CCPh)_4]$ (**2**), which is a vertex-missing Cu_{11} cuboctahedron encaging a PtH moiety, and $[PtH_2Cu_{11}\{S_2P(O^iPr)_2\}_6(CCPh)_3]$ (**3**), a distorted 3,3,4,4,4-pentacapped trigonal prismatic Cu_{11} cage enclosing a PtH_2 unit. The electronic structure of **2,** analyzed by Density Functional Theory, is a 2e superatom. The electrocatalytic activities of **1**-**3** for hydrogen evolution reaction (HER) were compared. Notably, Cluster **2** exhibited an exceptionally excellent HER activity within metal nanoclusters, with an onset potential of –0.03 V (at 10 mA cm^{-2}), a Tafel slope of 39 mV dec^{-1}, and consistent HER activity throughout 3000 cycles in 0.5 M H_2SO_4. Our study suggests that the accessible central Pt site plays a crucial role in the remarkable HER activity and may provide valuable insights for establishing correlations between catalyst structure and HER activity.

Introduction

Hydrogen has sparked the interest of many researchers as an important clean energy carrier. In order to achieve sustainable hydrogen production, it is crucial to create a synthetic catalytic system that can efficiently produce H_2. Many catalysts have been reported for the electro-catalytic hydrogen evolution reaction (HER).[1,2] Researchers have extensively investigated earth-abundant materials to apply HER on a large scale and in a sustainable manner.[3-6] However, none of these materials have surpassed the HER performance of Pt-based materials, which are commonly used.[7-10] Due to the high cost of platinum-based catalyst, there is a high demand for developing catalysts containing less platinum. HER electrocatalysts with unique properties can be developed by alloying two or more metals. Previous studies have established the benefits of alloying Pt with different metals for electro-catalytic HER.[11-14] Alloying with coinage metals, in particular has proven to be successful.[15] For example, $PtAu_{24}(SC_6H_{13})_{18}$ exhibits an improved HER performance, possibly due to Pt-H intermediate.[16] However, the instability of Pt-Au bimetallic clusters and the tendency of Au(I) to form Au(0) results in decomposition and prevents recyclability. We propose the synthesis of superatomic Pt-doped copper-rich hydride nanoclusters as ideal substitutes. These nanoclusters will contain the critical H-Pt fragment necessary for optimal HER characteristics such as durability, efficiency, and cost-effectiveness.[17-21] The size, composition, and structure of our bimetallic hydride clusters are controlled with atomic precision to exhibit optimal binding properties for HER.

Copper hydride nanoclusters (NCs) have a wide range of applications in natural products[22] and methodology development.[23-26] Our research group has previously reported several Cu(I) hydride clusters stabilized by 1,1-dithiolates such as $[Cu_7(H)L_6]$ and $[Cu_8(H)L_6]^+$,[27-30] $[Cu_{20}(H)_{11}L_9]$,[31] $[Cu_{28}(H)_{15}L_{12}](PF_6)$,[32] $[Cu_{27}(H)_{15}L_{12}]$,[33] $[Cu_{30}(H)_{18}L_{12}]$,[34] and $[Cu_{32}(H)_{20}L_{12}]$[35] (L = dichalcogenolate).[36] In this study, our goal is to enhance the HER activity performance in these copper hydride NCs by doping them with Pt. Recently, we developed a methodology that involves reacting large copper hydrides with terminal alkynes to generate a smaller cluster $[CuH_2@Cu_{14}L_6(C_2R)_6]^+$, where the 14 Cu(I) atoms feature a D_{3d} bicapped icosahedron that houses a $[CuH_2]^-$ unit at its center[37].

Additionally, we created the iso-structural bimetallic clusters $[MH_2@Cu_{14}L_6(C_2Ph)_6]^z$ (M= Pd, z = 0 and M =Ag; z = +1) by doping copper-rich hydrides templates with a foreign metal ion (Pd[38] and Ag[39]). Subsequently, we prepared $[PtH_2Cu_{14}(dtp)_6\{CCPh\}_6]$ (dtp = dithiophosphate) by using similar method and its structure was confirmed by both single-crystal X-ray and neutron diffraction. To the best of our knowledge, a linear PtH_2 unit inside a copper cage is still unknown, although one platinum-copper bimetallic cluster has been reported.[40]

In this study, we present the synthesis and structure of $[PtH_2Cu_{14}\{S_2P(O^iPr)_2\}_6(CCPh)_6]$ (**1**). Its crystal structure reveals a bicapped icosahedral copper(I) cage embedded in a linear platinum dihydride $[PtH_2]^{2-}$ unit. Upon the addition of two equiv. of CF_3COOH to **1**, we isolated $[PtHCu_{11}\{S_2P(O^iPr)_2\}_6(CCPh)_4]$ (**2**) and $[PtH_2Cu_{11}\{S_2P(O^iPr)_2\}_6(CCPh)_3]$ (**3**). The X-ray diffraction structures of **2** and **3** were resolved from the co-crystals $[PtHCu_{11}\{S_2P(O^iPr)_2\}_6(CCPh)_4]_2 \cdot [Cu_7(H)\{S_2P(O^iPr)_2\}_6]_{0.85} \cdot [Cu_7(Cl)\{S_2P(O^iPr)_2\}_6]_{0.15}$ ($[\mathbf{2}]_2 \cdot [\mathbf{4}]_{0.85} \cdot [\mathbf{5}]_{0.15}$) and $[PtH_2Cu_{11}\{S_2P(O^iPr)_2\}_6(CCPh)_3]_2 \cdot [Cu_7(H)\{S_2P(O^iPr)_2\}_6]_{0.75} \cdot [Cu_7(Cl)\{S_2P(O^iPr)_2\}_6]_{0.25}$ ($[\mathbf{3}]_2 \cdot [\mathbf{4}]_{0.75} \cdot [\mathbf{5}]_{0.25}$), respectively. Thus, $[PtH_2Cu_{14}\{S_2P(O^iPr)_2\}_6(CCPh)_6]$ (**1**) and $[PtH_2Cu_{11}\{S_2P(O^iPr)_2\}_6(CCPh)_3]$ (**3**) are neutral species, while $[PtHCu_{11}\{S_2P(O^iPr)_2\}_6(CCPh)_4]$ (**2**) is *two-electron superatomic alloy*. The addition of CF_3COOH to **1** induces a structural change from an HER-inactive NC to the HER-active cluster **2**, which exhibits the highest HER activity among the bimetallic NC catalysts. It has a near-zero onset potential (η) of -0.03 V (at 10 mA cm^{-2}), a Tafel slope of 39 mV dec^{-1}, and a Faradaic efficiency over 98%, resulting in a TOF value of 526 s^{-1} at η= 0.1 V.

Results and Discussion

Synthesis and Characterization

Cluster **1** was successfully prepared by reacting the precursor $[Cu_{20}H_{11}\{S_2P(O^iPr)_2\}_9]$[31] with $[Pt\{S_2P(O^iPr)_2\}_2]$[41] in the presence of phenylacetylene in THF at ambient temperature for 48 hours (Scheme S1a). After workup, a yield of 15 % was obtained. The reduction of Pt(II) to Pt(0) in complex **1** is attributed to the hydrides in the copper precursor. The deuteride analogue $[PtD_2Cu_{14}\{S_2P(O^iPr)_2\}_6(CCPh)_6]$ (**1D**, Yield: 16 %) was obtained from the $[Cu_{20}D_{11}\{S_2P(O^iPr)_2\}_9]$ precursor using the same protocol. Alternatively, the reaction of $[Cu_{11}H_2\{S_2P(O^iPr)_2\}_6(CCPh)_3]$[42] with $[Pt\{S_2P(O^iPr)_2\}_2]$ in an equimolar ratio resulted in the formation of **1** with an 11% yield (Scheme S1b). By using the one-pot reaction method of $[Cu(CH_3CN)_4](PF_6)$, $[NH_4][S_2P(O^iPr)_2]$, $[BH_4]^-$, $[Pt\{S_2P(O^iPr)_2\}_2]$, and phenylacetylene along with NEt_3, where the mole ratios of 7:3:2:1:4:4 at 0°C under N_2 conditions, the yield can be improved up to 17 % (Scheme S1c).

The composition of **1** was initially characterized by positive mode ESI-MS analysis (Figure 1a). The spectrum shows a clearly dominant peak centered at *m/z* 2971.31 with one positive charge due to the formation of the protonated adduct, $[\mathbf{1_H}+H^+]^+$ (calcd. *m/z* 2971.33 Da). The isotopic pattern excellently agrees with the simulation (Figure 1a, Inset). The deuteride analogue **1D** produces an identical fragmentation pattern with a peak at *m/z* 2973.41 (calcd. *m/z* 2973.35 Da), corresponding to $[\mathbf{1_D}+H^+]^+$ (Figure S1). The theoretical isotopic pattern of $[\mathbf{1_D}+H^+]^+$ also excellently agrees with the experiment (Figure S1, Inset).

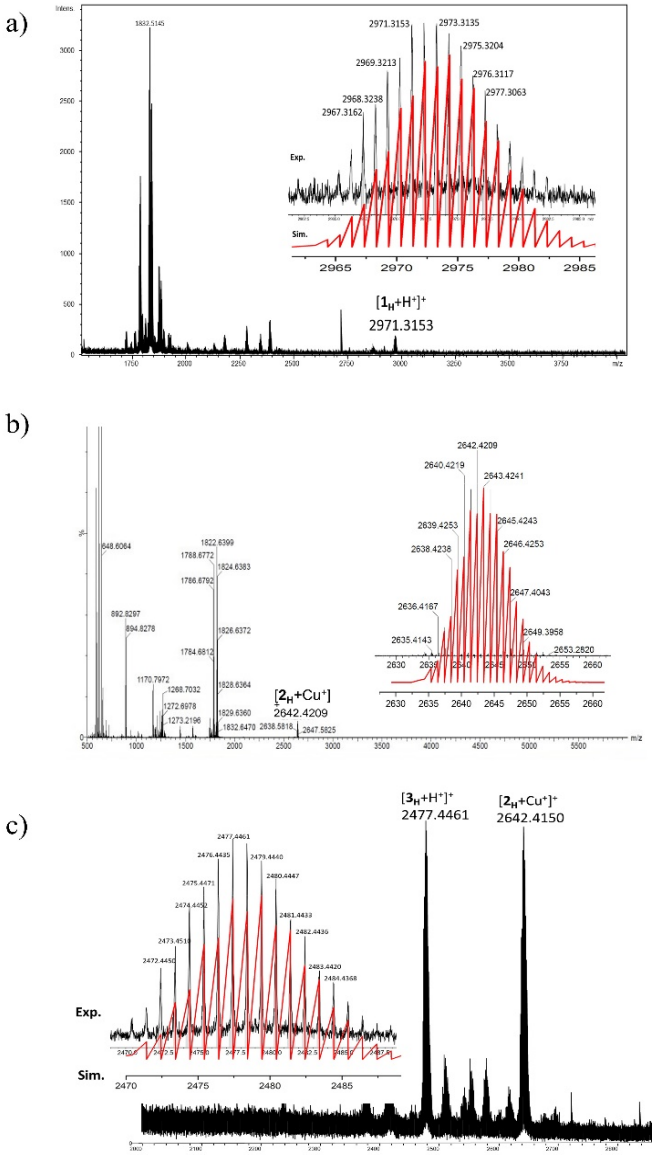

Figure 1. Positive ESI-MS spectra of the clusters of a) $[\mathbf{1_H}+H^+]^+$, b) $[\mathbf{2_H}+Cu^+]^+$, and c) $[\mathbf{3_H}+H^+]^+$. The inset shows the isotope pattern of the experimental (top) and simulated (bottom) isotope patterns.

The $^{31}P\{^1H\}$ NMR spectrum of **1** displays a single resonance at 102.5 ppm (Figure S2). The ^1H NMR spectrum shows two sets of peaks for the dtp and one set for the alkynyl ligands (Figure S3). The resonance of its two hydrides is around 0.50 ppm in $CDCl_3$ with a $J_{Pt\text{-}H}$ coupling constant of 712.2 Hz. This is confirmed by a simulated spectrum (Figure S4), which assumes the hydride position at 0.58 ppm with a scalar coupling constant of 710 Hz. Meanwhile, the presence of the two hydrides is supported by $^1H\{^{195}Pt\}$ 1D-HMQC, echoed at 0.48 ppm (Figure S5), and the $^1H\{^{195}Pt\}$ 1D-HMQC without decoupling shows a doublet peak with a $J_{Pt\text{-}H}$ coupling constant of 704.82 Hz (Figure S6). In addition, the ^{195}Pt NMR spectrum (Figure S7) depicts a peak at -4875.3 ppm close to the ^{195}Pt NMR of Pt(0) in $[Pt(PMe_2Ph)_4]$ (δ_{Pt} = -4728 ppm) and [Pt(1.5-cyclooctadiene)$_2$] (δ_{Pt} = -4636 ppm).[43] The

presence of two hydrides in **1** is further confirmed by the ^{2}H NMR spectrum of its deuteride analogue **1$_D$**, which shows a signal at 0.64 ppm in $CHCl_3$ (Figure S8). The elemental analysis further confirmed the purity of **1**. The carbon and hydrogen contents are 32.01% and 3.73%, respectively, close to the theoretical values (C:33.93%, and H: 3.93%).

We investigated the reactivity of cluster **1** upon the addition of two equiv. of CF_3COOH at ambient temperature, generating in a novel cluster $[PtHCu_{11}\{S_2P(O^iPr)_2\}_6(CCPh)_4]$ (**2**) with a 19 % yield (Scheme S1d). This acid treatment also generates another cluster, $[PtH_2Cu_{11}\{S_2P(O^iPr)_2\}_6(CCPh)_3]$ (**3**) with a 12% yield. Clusters **2** and **3** exhibit different solubility in methanol, allowing for easy separation.

Cluster **2** is a neutral cluster containing a Pt(0) atom at its center. The neutrality of the cluster is confirmed by ESI-MS spectrometry, which shows a peak at *m/z* 2642.42 Da in the positive ion mode (Figure 1b), corresponding to the formation of a Cu adduct, $[\mathbf{2_H}+Cu^+]^+$ (calcd. *m/z* 2642.38 Da). The experimental isotopic distribution of the peaks (top) matches well with simulation distribution (bottom) (Figure 1b, Inset). The positive-ion ESI-MS spectrum of the deuteride analogue **2$_D$** exhibits a peak at *m/z* 2643.40 Da, which corresponds to the $[\mathbf{2_D}+Cu^+]^+$ (calcd. *m/z* 2463.39 Da) (Figure S9). The purity of **2** was determined via accurate elemental analysis, which showed carbon and hydrogen contents of 30.67% and 4.69%, respectively. These values are close to the theoretical values (C: 31.67% and H: 4.10%).

The $^{31}P\{^{1}H\}$ NMR spectrum of **2** shows five peaks at 93.4, 96.5, 98.1, 100.4, and 103.9 ppm, which are significantly shifted upfield compared to cluster **1** (102.5 ppm) (Figure S10). The ^{1}H NMR analysis identified the alkynyl and dtp ligands (Figure S11). The hydride displays a single peak at 4.35 ppm in d_6-acetone ($J_{Pt\text{-}H}$= 880 Hz) and correlates well with the simulated ^{1}H NMR spectrum of $^{1}H\{^{195}Pt\}$ nuclei (Figure S12). The ^{195}Pt NMR chemical shift -4962.34 ppm (see Figure S13) is close to the ^{195}Pt NMR of cluster **1**. These spectral patterns suggest that acid addition to **1** resulted in structural change from D_{3d} to C_1 symmetry.

The composition of **3** was verified by ESI-MS analysis (Figure 1c). It displays two prominent peaks at *m/z* 2477.41 and 2642.42 Da in the positive ion mode (Figure 1c). The former peak corresponds to the formation of the protonated adduct, $[\mathbf{3_H}+H^+]^+$ (calcd. *m/z* 2477.43 Da), and the latter corresponds to the Cu adduct with an additional alkynyl ligand. This is further confirmed by matching the experimental (black trace) and simulated (red trace) isotopic distribution of the peaks (Figure 1c, Inset). Furthermore, the ESI-MS analysis of the deuteride analogue [**3$_D$**] confirmed the presence of two deuterides as indicated by a peak at *m/z* 2543.99 Da (calcd. *m/z* 2543.36 Da) (Figure S14), which can be assigned to $[\mathbf{3_D}+Cu^+]^+$. The simulation and experiment isotopic patterns resemble those in Figure S14, inset. The purity of **3** was confirmed via elemental analysis, with carbon, sulphur, and hydrogen contents of 28.78 %, 15.09 %, and 3.95 %, respectively, which are close to the theoretical values (29.07 %, 15.52 %, and 4.11 %).

The $^{31}P\{^{1}H\}$ NMR spectrum of **3** reveals a single peak at 100.2 ppm (Figure S15). Its ^{1}H NMR spectrum shows two sets of peaks for the dtp ligands and one set for the alkynyl ligands (Figure S16). The two hydrides are associated with a peak at 2.35 ppm in $CDCl_3$ accompanied with a platinum satellite, $J_{Pt\text{-}H}$ = 732 Hz. The presence of the two hydrides is confirmed by $^{1}H\{^{195}Pt\}$ 1D-HMQC with decoupling at a peak of 2.34 ppm (Figure S17). Moreover, the $^{1}H\{1^{95}Pt\}$ 1D-HMQC without decoupling shows a doublet peak with the $J_{Pt\text{-}H}$ coupling constant of 729 Hz (Figure S18). The ^{195}Pt NMR spectrum shows an intense peak at -4855.46 ppm (Figure S19), close to the ^{195}Pt NMR of cluster **1**. The ^{2}H NMR spectrum of its deuteride analogue **3$_D$** shows a signal at 2.45 ppm in $CHCl_3$ (Figure S20).

X-ray Structure Analysis

The molecular representation of cluster **1** is shown in Figure 2a. Selected bond lengths and angles are provided in Table 1 and the crystallographic data in Table S1. The triclinic $P\bar{1}$ unit cell contains two halves of symmetry-independent molecules. Both molecules are centrosymmetric and have similar metrical data (Table 1). The metal framework of **1** consists of a Pt-centered Cu_{12} icosahedron capped by opposite faces of two Cu atoms (Figure 2b). Two hydrides are located in the interstitial cavities, forming a linear H-Pt-H motif along the C_3 axis. The interstitial hydrides are in a trigonal pyramidal (*tp*) coordination mode, connected to Pt and three Cu_{core} forming an icosahedral triangular face.

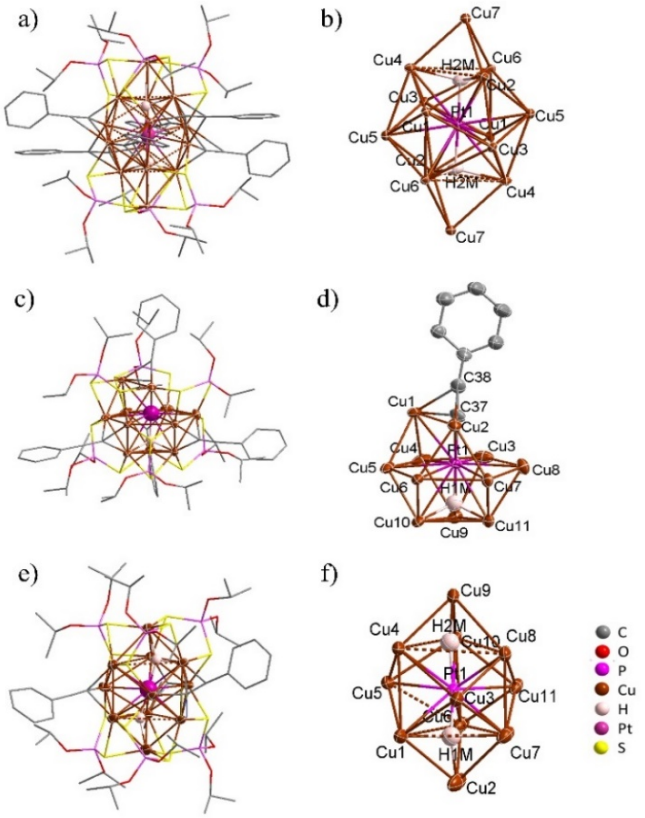

Figure 2. a) The whole structure of **1**. (b) The Cu_{14} bicapped icosahedral framework of **1$_N$** houses a linear PtH_2 unit with interstitial hydride atoms in a trigonal-pyramidal coordination mode. c) The whole structure of **2**. d) $PtHCu_{11}$ framework in **2** with the insertion of an alkynyl ligand. e) Total structure of **3**. f) The 3,3,4,4,4-trigonal-prismatic geometry shell structure of **3** houses a linear PtH_2 unit. Thermal ellipsoids at 50% probability. All H atoms except hydrides are omitted for clarity.

Table 1. Selected measured bond lengths (Å) for **1**, **1$_N$**, **2**, and **3**.

	1[a]		**1$_N$**[b]		**2**[a]	**3**[a]
Pt_{cent}-Cu	2.6866(4)-2.8187(5), avg. 2.7453(4)	2.7007(4)-2.8257(4), avg. 2.7601(4)	2.6881(19)-2.8167(19), avg. 2.749(2)	2.715(2)-2.831(2), avg. 2.763(4)	2.6768(13)-3.000(2), avg. 2.838(2)	2.6836(13)-2.6616(12) avg. 2.6696(13)
Cu_{core}-Cu_{core}[c]	2.5791(6)-2.7775(6), avg. 2.6800(6)	2.6109(6)-2.7667(6), avg. 2.6654(6)	2.573(3)-2.775(3), avg. 2.682(3)	2.615(3)-2.765(3), avg. 2.668(3)	2.544(2)-2.7357(18), avg. 2.644(2)	2.5703(18)-3.0026(16) avg. 2.8014(16)
Cu_{cap}-Cu_{core}[c]	2.7178(6)-2.7980(6), avg. 2.7579(6)	2.7557(6)-2.7668(6), avg. 2.7613(6)	2.715(3)-2.791(3), avg. 2.753(3)	2.766(3)-2.767(3), avg. 2.767(3)		2.7833(18)-2.9414(16) avg. 2.839(14)
Pt_{cent}-H	1.62(4)	1.74(4)	1.725(5)	1.734(5)	1.714(9)	1.670(10)-1.695(10) avg. 1.683(10)
Cu_{cap}-H						1.78(6)-1.79(10) avg. 1.785(8)
Cu_{core}-H[c]	1.80(3)-2.05(3), avg. 1.92(3)	1.79(4)-1.92(4), avg. 1.88(4)	1.881(6)-1.896(6), avg. 1.886(6)	1.860(6)-1.892(6), avg. 1.878(6)	1.782(9)-1.784(9), avg. 1.783(9)	1.74(10)-2.07(10) avg. 1.90(10)
Cu-S	2.2628(9)-2.4794(10), avg. 2.3699(9)	2.2550(10)-2.4620(9), avg. 2.3772(10	2.259(6)-2.475(6) avg. 2.372(6)	2.252(6)-2.478(6), avg. 2.380(6)	2.254(3)-2.415(3), avg. 2.333(3)	2.295(4)-2.448(3) avg. 2.348(3)
Cu-C	1.936(3)-2.138(3), avg. 2.065(3)	1.918(4)-2.181(3), avg. 2.067(3)	1.933(3)-2.141(3) avg. 2.063(3)	1.914(3)-2.195(3), avg. 2.067(3)	1.973(12)-2.084(11), avg. 2.029(11)	1.954(10)-2.155(9) avg. 2.061(10)
C≡C	1.211(5)-1.227(5), avg. 1.217(5)	1.211(6)-2.228(5), avg. 1.222(5)	1.230(3)-1.245(3) avg. 1.239(3)	1.228(4)-1.241(3), avg. 1.235(3)	1.201(15)-1.244(16), avg. 1.220(15)	1.173(14)-1.210(13) avg. 1.195(14)
Pt-C					2.030(12)	
S…S bite	3.415(1)-3.457(1), avg. 3.433(1)	3.422(1)-3.424(1), avg. 3.423(1)	3.419(9)-3.444(8), avg. 3.433(8)	3.410(8)-3.442(7), avg. 3.422(8)	3.416(6)-3.475(4), avg. 3.282(5)	3.456(4)-3.485(4) avg. 3.471(4)

[a] X-ray data. [b] Neutron data. [c] Core: icosahedron (**1**), vertex missing cuboctahedron (**2**), and trigonal prism (**3**).

The PtH_2Cu_{14} framework has approximate D_{3d} symmetry and is protected by six $PhC{\equiv}C^-$ and six dtp ligands. The alkynyl ligands are connected in μ_3-η^1 fashion on the trigonal faces alternating along the waist of the Cu_{12} icosahedron. The dtp ligands are located at both ends of the PtH_2Cu_{14} framework, bridging the butterflies formed by one Cu_{cap} and three Cu_{core} atoms in a (μ_2, μ_2) binding mode. Thus, the ideal symmetry of the entire cluster is lowered to S_6 due to the ligand arrangement. The hydride position in **1** was further confirmed by high-resolution neutron diffraction (structure **1$_N$** in Table 1). To the best of our knowledge, this is the first example of a trigonal-pyramidal hydride coordination mode in a $PtCu_3$ cavity evidenced by neutron diffraction. The hydride positions in **1$_N$** are relatively close to those found in the X-ray structure, with average Pt-H and Cu_{core}-H distances of 1.734(5) and 1.878(6) Å, respectively. The structure of **1** is similar to that of its isoelectronic relative $[PdH_2Cu_{14}\{S_2P(O^iPr)_2\}_6(C_2Ph)_6]$[38] with μ_4-H in *tp* geometry. It is noteworthy noting that in the dithiocarbamate (dtc) homologue $[PdH_2Cu_{14}\{S_2CN^nBu_2\}_6(C_2Ph)_6]$,[38] the hydrides are in a μ_5-H trigonal bipyramidal (*tbp*) geometry, being also bonded to their Cu_{cap} neighbors. This difference results from the different bite effects of the dtp and dtc ligands (average S···S bite distance = 3.43 and 3.05 Å, respectively).

The molecular structure of **2** was determined by an X-ray diffraction analysis of a co-crystal. This co-crystal consists of $[PtHCu_{11}\{S_2P(O^iPr)_2\}_6(CCPh)_4]_2 \cdot [Cu_7(H)\{S_2P(O^iPr)_2\}_6]_{0.85} \cdot [Cu_7(Cl)\{S_2P(O^iPr)_2\}_6]_{0.15}$ ([**2**]$_2$·[**4**]$_{0.85}$·[**5**]$_{0.15}$) and crystallizes in the $P\bar{1}$ space group. The visual metal framework reveals that it has a Pt-centered cuboctahedron with a missing vertex. It has a C_1 symmetry and is capped by six dtp ligands on the square faces and four alkynyl ligands on the four triangular faces arranged in a tetrahedral manner (Figure 2c). It is worth noting that a similar vacancy defect *fcc* structure was observed in the previously reported $[AuCu_{11}\{S_2P(O^iPr)_2\}_6(CCPh)_3Cl]$[39] and the strongly related $[PdHCu_{11}\{S_2P(O^iPr)_2\}_6(CCPh)_4]$.[15] These clusters can be compared to their homologues $[MCu_{12}\{S_2P(O^iPr)_2\}_6(CCPh)_4$ (M = Cu, Ag, Au)[44-46], which have a complete cuboctahedral (perfect

fcc) structure. This vacancy defect allows the insertion of one alkynyl ligand on a cuboctahedral triangular face (Figure 2d), leading to the formation of a short Pt-C37 contact of 2.030(12) Å. Therefore, the alkynyl ligand (on C37) shows a μ_3: η^2, η^2, η^1 binding fashion, connecting to the center Pt and two Cu_{core} atoms via σ bonding (C37-Cu_{core}: 2.021(12) and 2.028(11) Å) and π bonding (C38-Cu_{core}: 2.308(12) and 2.61(1) Å). In contrast, the other three alkynyl ligands show two μ_3: η^1, η^1, η^1 and one μ_3: η^2, η^1, η^1 fashions with an average C(σ)-Cu_{core} distance of 2.029(11) Å (1.973(12)-2.084(11) Å) and a C(π)-Cu_{core} distance of 2.438(11) Å. The hydride is located in a tetrahedral cavity formed by Pt1 and the Cu9, Cu10, and Cu11 cuboctahedron triangular face. Consequently, the hydride is positioned *trans* to C37 (C37-Pt1-H1M = 176.0(4)°). The average distances of Pt-H and Cu_{core}-H are 1.714 (9) Å and 1.783(9) Å, respectively. The hydride-connected triangular face composed of Cu9, Cu10, and Cu11 is slightly expanded (average Cu…Cu = 2.8368(18) Å compared to 2.7608(18) and 2.770(2) Å for the other alkynyl-free triangular faces). Overall, the structure of cluster **2** is similar to that of its Pd relative $[PdHCu_{11}\{S_2P(O^iPr)_2\}_6(CCPh)_4]$.[15] The other clusters present in the co-crystal, namely $[Cu_7(H)\{S_2P(O^iPr)_2\}_6]$ (**4**) and $[Cu_7(Cl)\{S_2P(O^iPr)_2\}_6]$ (**5**), have been previously reported.[30,42,47]

The molecular structure of **3** was determined by X-ray diffraction analysis of a co-crystal of $[PtH_2Cu_{11}\{S_2P(O^iPr)_2\}_6(CCPh)_3]_2 \cdot [Cu_7(H)\{S_2P(O^iPr)_2\}_6]_{0.75} \cdot [Cu_7(Cl)\{S_2P(O^iPr)_2\}_6]_{0.25}$ ($[\mathbf{3}]_2{\cdot}[\mathbf{4}]_{0.75}{\cdot}[\mathbf{5}]_{0.25}$) that also crystallizes in the $P\bar{1}$ space group. The structure of **3** (Figure 2e) is similar to its isoelectronic relative $[CuH_2Cu_{11}\{S_2P(O^iPr)_2\}_6(CCPh)_3]^+$,[39] but the metallic framework more distorted. In the X-ray structure of the homometallic cluster, the CuH_2Cu_{11} core has D_{3h} symmetry and reveals a Cu_{11} 3,3,4,4,4-pentacapped trigonal prism encapsulating a linear CuH_2 unit, with the Cu atom positioned at the center of the trigonal prism. The hydrides are located on the C_3 axis and are strongly bonded to the central atom. They also interact with the Cu_3 bases of the trigonal prisms and cap Cu atom, resulting in a trigonal bipyramidal (*tbp*) μ_5-H coordination mode. The PtH_2Cu_{11} core of **3** can also be described as a Cu_{11} pentacapped trigonal prism that encloses a PtH_2 unit. However, the trigonal prism is significantly distorted in a manner that the hydrides are no longer in a symmetrical *tbp* coordination mode (Figure 2f). One of the hydrides (μ_3-H) is found lying in an approximate trigonal planar coordination mode, connected to Pt, only one Cu of a Cu_3 triangular base and its capping atom. The other hydride (μ_4-H) is connected to Pt, two Cu atoms of a Cu_3 base and its capping atom in a seesaw (or flattened tetrahedral) geometry. The distortion away from D_{3h} also causes some bending of the PtH_2 unit (H-Pt-H = 170°). The ligand environment in **3** is similar to that in $[CuH_2Cu_{11}\{S_2P(O^iPr)_2\}_6(CCPh)_3]^+$,[39] with the six dtp ligands capping four copper atoms in a (μ_2, μ_2) mode and the three alkynyl ligands arranged along the waist of the pentacapped prism in a (μ_3-η^1) fashion.

The co-crystals $[\mathbf{2}]_2{\cdot}[\mathbf{4}]_{0.85}{\cdot}[\mathbf{5}]_{0.15}$ and $[\mathbf{3}]_2{\cdot}[\mathbf{4}]_{0.75}{\cdot}[\mathbf{5}]_{0.25}$ were further characterized by $^{31}P\{^1H\}$ NMR spectroscopy. As shown in Figure S21, the former shows eight peaks at 102.2, 99.9, 98.4, 97.1, 95.3, 95.2 (**2**), 102.7 (**4**), and 97.2 (**5**). The ^1H NMR resonances at 4.26 and 3.57 ppm precisely match the expected 1:0.48 hydride ratio (Figure S22). The latter co-crystal displays three peaks in the $^{31}P\{^1H\}$ NMR spectrum, centered at 100.1 (**3**), 102.2 (**4**), and 97.1 (**5**) ppm in ratios of 1:0.34:0.12 (Figure S23). The overall composition of $[\mathbf{2}]_2{\cdot}[\mathbf{4}]_{0.85}{\cdot}[\mathbf{5}]_{0.15}$ and $[\mathbf{3}]_2{\cdot}[\mathbf{4}]_{0.75}{\cdot}[\mathbf{5}]_{0.25}$ was further characterized by ESI-mass spectrometry (Figures S24 and S25).

UV-vis Absorption

The UV-Vis absorption spectra of **1**, **2**, and **3** are shown in Figure S26a. Cluster **1** displays optical absorption bands at 316, 472, 528, and 608 nm. The acid treatment of cluster **1** does affect the optical properties. The characteristic absorption peaks of cluster **2** are at 327, 414, and 533 nm, while cluster **3** has peaks at 318, 435 and 538 nm. The absorption bands of **2** and **3** show a significant hypochromic shift compared to **1**. This result indicates that controlling the size and structure of these bimetallic hydride clusters influences their optical properties.

Electrochemical Hydrogen Evolution Reaction (HER)

The electrocatalytic HER activities of clusters **1**, **2**, and **3** were examined by obtaining linear sweep voltammograms (LSVs) in a three-electrode electrochemical cell containing deaerated 0.5 M H_2SO_4 (see Experimental section for details). The cluster-immobilized working electrodes were fabricated by dropcasting a cluster solution onto carbon paper (PtH_2Cu_{14}/C, $PtHCu_{11}$/C and PtH_2Cu_{11}/C). The LSVs in Figure 3a show that cluster **2** exhibited much higher HER activity than **1** and **3**, and produces hydrogen at near-zero overpotential vs. reversible hydrogen electrode (RHE). [Hereafter, all potentials are reported vs. RHE unless noted otherwise.] As shown in Figure 3a, the HER activity of the carbon paper was negligible, suggesting that the HER current was mainly from the clusters. The onset potentials for the current density of 10 mA cm^{-2} were –0.40, –0.03, and –0.28 V for **1**, **2**, and **3**, respectively, indicating that cluster **2** is a highly efficient H_2-producing electrocatalyst. The onset potential is comparable to that of the benchmark Pt/C catalyst (–0.01 V).

Analysis of the gaseous products produced from controlled potential electrolysis measurements of cluster **2** using online gas chromatography revealed that the faradaic efficiency for H_2 was over 98 % at all potentials, indicating that the generated charges were exclusively used for H_2 production (Figure 3b). Additionally, the square wave voltammograms (SWV) of CH_2Cl_2 solutions of **1**, **2** and **3** exhibit well-resolved current peaks that lie at the formal potentials of the cluster charge-state couples (Figure 3c). Comparison of the formal potentials with the thermodynamic reduction potential of proton in 0.5 M H_2SO_4 (–0.66 V vs. $Fc^{0/+}$) revealed that clusters **1**, **2** and **3** maintained their original neutral charge states during the electrocatalytic HER.

To understand the origin of the significantly different HER activities observed for these clusters, we conducted analyses in a kinetically controlled regime. As shown in Figure 3d, the Tafel slope obtained for cluster **2** is significantly different from those obtained for **1** and **3**, suggesting that the HER occurs via a distinctly different pathway on cluster **2**. In other words, the high Tafel slopes (156 and 209 mV dec^{-1}) observed for clusters **1** and **3**, respectively, suggest that the HER processes are gated by the hydrogen adsorption step (the Volmer pathway). However, in cluster **2**, the Tafel slope was dramatically reduced to 39 mV dec^{-1}, indicating that the hydrogen adsorption step was greatly facilitated and the HER occurs via the Volmer–Heyrovsky pathway.[48] It is worth noting that the benchmark Pt/C exhibits a smaller Tafel slope of 31 mV dec^{-1}, indicating that H_2 evolution occurs through the coupling of two adjacent H atoms adsorbed on Pt surface (the Volmer-Tafel pathway).

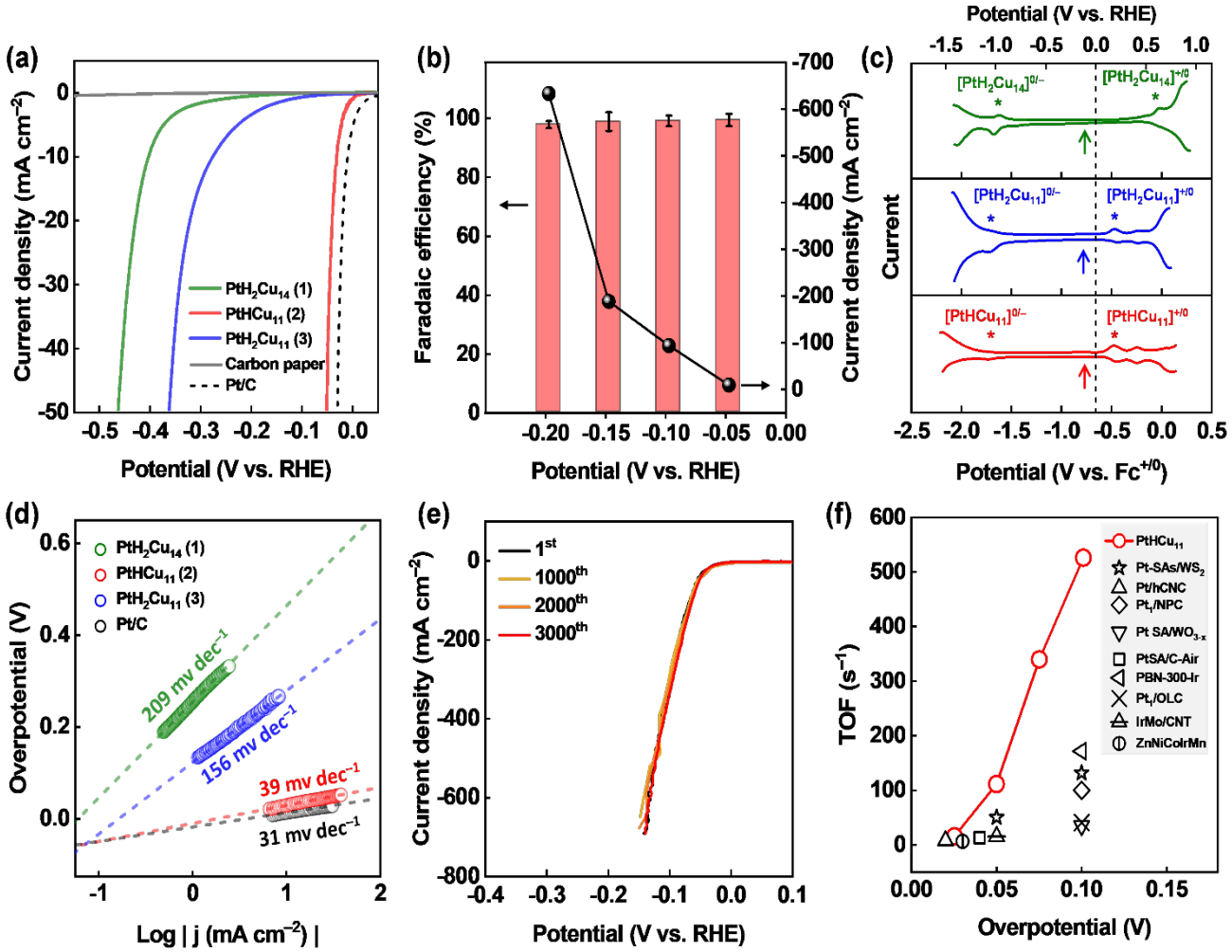

Figure 3. a) LSVs recorded at 1 mV s^{-1} on clusters **1, 2, 3** and Pt/C. b) Faradaic efficiencies and current densities for H_2 production measured for cluster **2** at various applied potentials. c) SWVs of CH_2Cl_2 solutions of cluster **1**, **2**, and **3**, where *denotes the first oxidation and reduction peaks. Arrows indicate the open-circuit potentials. d) Tafel plots for HER on cluster **1**, **2**, and **3**. e) Cyclic voltammograms recorded at 50 mV s^{-1} on cluster **2** during 3000 cycles. e) Comparison of TOF values for H_2 production determined for cluster **2** (red circles) with other electrocatalysts (Table S3). All potentials were *iR*-corrected except those in (c).

The Tafel slope analysis clearly reveals the relationship between the structure and the HER activity for the three Pt-doped Cu-rich clusters. Although proton access to the catalytically active Pt site is significantly blocked by the complete Cu_{14} and Cu_{11} cages in clusters **1** and **3**, respectively, the vertex-missing Cu_{11} cuboctahedron cage in cluster **2** allows easy access of the proton to the Pt site, greatly facilitating the Volmer step. However, the central Pt site in cluster **2** only allows singly adsorbed hydrogen, which subsequently reacts with the incoming proton to release H_2 (the Volmer–Heyrovsky pathway) instead of the Volmer-Tafel pathway.

Cluster **2** can be thought of as a Pt atom stabilized in a defective cuboctahedron, allowing the reactant access to the catalytic site. As shown in Figure 3e, cluster **2** exhibited consistent HER activity during 3000 cycles, demonstrating highly durable HER activity in acidic media. It has the best activity, compared to other HER electrocatalysts bimetallic clusters (Table S2). Additionally, it has a turnover frequency (TOF) value of 526 s^{-1} for H_2 production at 0.1 V, which is higher than those obtained from most efficient single-atom catalysts under similar conditions (Figure 3f and Table S3). Evidently, the vertex-missing Cu_{11} cuboctahedron encaging a PtH moiety provides a set of design principles for developing efficient HER electrocatalysts.

Computational Investigation

Density functional theory (DFT) calculations were performed at the PBE0/Def2TZVP level (see Computational Details section) on simplified models of **1**, **2**, and **3**. In these models, the O^{i}Pr groups in the dtp ligands were replaced with H in order to reduce computational cost. This simplification has been justified in previous studies. [27,30-32,34-40,44-49] The frontier Kohn-Sham orbital diagrams for these models are shown in Figure 4 and selected computed metrical data and Wiberg indices are presented in Table 2. The optimized geometries of clusters **1-3** are in good agreement with their experimental structures (compare Tables 1 and 2). Notably, DFT unambiguously confirms the location of the hydrides in **2** and **3** as determined by X-ray diffraction analyses. This includes the unsymmetrical and different coordination modes of the two hydrides in **3** (see above) and the optimized H-Pt-H

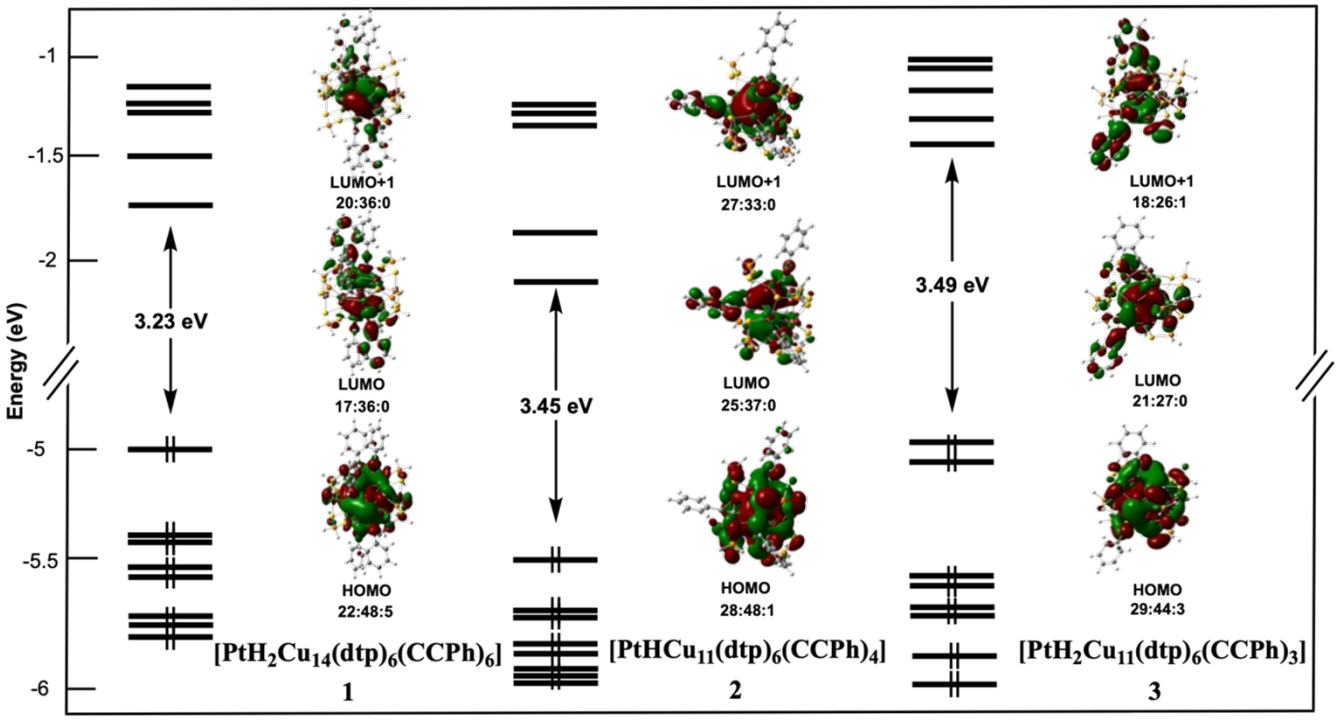

Figure. 4. Kohn-Sham orbital diagrams of **1, 2**, and **3** clusters. Orbital localization (%) are given in the order Pt/Cu/H.

angle (168° (DFT) *vs.* 170° (X-ray)). It should be noted that the distorted optimized geometry of **3** was obtained from a symmetrical structure resembling that of the isoelectronic relative $[CuH_2Cu_{11}\{S_2P(O^iPr)_2\}_6(CCPh)_3]^+$.[39] Thus, substituting the central Cu^+ ion in the former cluster by a much larger Pt(0) atom to form **3** significantly distorts the entire molecular framework from C_{3h} to C_1 symmetry.

In the three clusters, the Pt-H Wiberg bond indices are much larger than the Cu-H ones (Table 2). This indicates that Pt-H bonds are significantly stronger. Considering the natural atomic charge distributions given in Table 3, clusters **1** and **3** can be described as ligated $[Cu_{14}]^{14+}$ and $[Cu_{11}]^{11+}$ cages, respectively, encapsulating a (nearly) linear $[PtH_2]^{2-}$ 14-electron complex.[38,39] The interaction between cage and guest has significant ionic character as evidenced by the PtH_2 computed natural charges, which are close to -2 (Table 3). By applying the same logic and examining the charge distribution in **2**, one can attribute a formal charge of -1 to the PtH unit and view the entire structure as a ligated $[Cu_{11}]^{11+}$ cage encapsulating a $[PtH]^-$ unit. $[PtH]^-$ has two occupied σ-type valence orbitals. One is the low-lying bonding orbital associated with the Pt-H electron pair with a dominant contribution from $5d_{z2}$(Pt) and a secondary contribution from 6s(Pt) character. The other valence orbital is the HOMO, a non-bonding 6s/$5d_{z2}$(Pt) hybrid of large 6s(Pt) component. This later orbital constitutes the major component of the HOMO of cluster **2**. In the related Pd derivative $[PdHCu_{11}\{S_2P(O^iPr)_2\}_6(CCPh)_4]$, this orbital has been described as the 1S orbital of a superatom with $1S^2\ 1P^0$ configuration, due to its significant 6s(Pd) character, as well as some 4s/4p(Cu) admixture.[15] The same situation holds for **2**, which can also be viewed as a 2-electron superatom with a 1S HOMO. This is supported by the fact that removing the encapsulated hydride as a proton from **2** generates the 2-electron anion $[PtCu_{11}\{S_2P(O^iPr)_2\}_6(CCPh)_4]^-$, which adopts a structure similar to **2** and whose 1S HOMO-2 resembles that of **2** (Figure S27). This hypothetical model is very similar to the real defective cuboctahedral $[AuCu_{11}\{S_2P(O^iPr)_2\}_6(CCPh)_3Cl]$ 2-electron cluster,[39] which also has a very similar 1S HOMO. Thus, there are (at least[15]) two possible qualitative descriptions of the electronic structure of **2** (the ionic host/guest approach and the superatom approach), each capturing some aspects of the wavefunction physics. The question then is: How about clusters **1** and **3**, which have been described as stable $[PtH_2]^{2-}$ anions encapsulated within a $[Cu_{14}]^{14+}$ cage? Would it also be possible to view them as superatoms? In searching for Kohn-Sham orbitals with sufficient 6s(Pt) and/or 4s(Cu) character (*i.e.,* orbitals that can be viewed as superatomic orbitals), only the HOMO's could be found, which actually resemble that of **2** (Figure 4). These HOMOs are largely composed of the HOMO-2 of the $[PtH_2]^{2-}$ unit, which is a non-bonding σ_g orbital made of the 6s(Pt) (primarily) and 5d(Pt) (secondarily) AOs. These features, together with the analysis of their lowest vacant orbitals (Figure 4), suggest viewing **1** and **3** as elongated (prolate) 2-electron NCs ($1S^2\ 1P^0$ configuration). However, when the two encapsulated hydrides are removed as protons from **1** and **3**, the resulting hypothetical dianions $[PtCu_{14}\{S_2P(O^iPr)_2\}_6(CCPh)_6]^{2-}$ and $[PtCu_{11}\{S_2P(O^iPr)_2\}_6(CCPh)_3]^{2-}$, adopt a structure similar to **1** and **3**, but are now clearly 4-electron oblate NCs (see Figures S28 and S29), with a superatomic configuration of $1S^2\ 1P_z^2\ 1P_x^0\ 1P_y^0$ (z axis // H-Pt-H vector). The two $1P_z$ electrons now occupy an orbital with a large Cu character that is empty in the **1** and **3** precursors. It should be noted that these dianionic species have significantly smaller HOMO-LUMO gaps than their protonated counterparts and therefore are highly hypothetical.

Time-dependent density functional theory (TD-DFT) calculations (see Computational details) was used to successfully simulate the UV-vis spectra of clusters **1**-**3** (Figure S26b). In all

Table 2. Selected DFT-computed averaged bond lengths (Å) and corresponding Wiberg bond indices into brackets for **1**, **2**, and **3**.

	Pt_{cent}-Cu	Cu_{core}-Cu_{core} [a]	Cu_{cap}-Cu_{core} [a]	Pt_{cent}-H	Cu_{cap}-H	Cu_{core}-H [a]	Cu-S	Cu-C	C≡C	Pt-C
1	2.773 [0.060]	2.917 [0.038]	2.807 [0.053]	1.725 [0.310]	2.343 [0.021]	1.951 [0.060]	2.397 [0.152]	2.064 [0.168]	1.235 [1.626]	
2	2.875 [0.041]	2.770 [0.035]		1.677 [0.380]		1.827 [0.049]	2.370 [0.164]	2.048 [0.172]	1.235 [2.625]	2.000 [0.491]
3	2.803 [0.037]	3.636 [0.010]	2.896 [0.027]	1.667 [0.368]	1.778 [0.063]	2.008 [0.044]	2.389 [0.157]	2.059 [0.182]	1.241 [2.627]	

[a] core = icosahedron (**1**), defect cuboctahedron (**2**), trigonal prism (**3**).

three clusters, the weak absorption band (or shoulder) of lowest energy is associated with a HOMO→LUMO transition, indicating a large MMCT nature, with some MLCT admixture. The other two main absorption bands in all three clusters are predominantly MLCT character.

Table 3. Selected computed data for **1**, **2** and **3**.

	1	**2**	**3**
HOMO-LUMO gap (eV)	3.23	3.45	3.55
Averaged NAO charges			
Pt	-0.79	-0.58	-0.80
H	-0.49	-0.48	-0.47
PtH/PtH_2	-1.77	-1.06	-1.74
Cu_{core} [a]	0.80	0.76	0.79
Cu_{cap}	0.70		0.75

[a] core = icosahedron (**1**), defect cuboctahedron (**2**), trigonal prism (**3**).

In our previous investigation on the HER electrocatalytic properties of the related $[PdHCu_{11}\{S_2P(O^iPr)_2\}_6(CCPh)_4]$, our calculations showed that the first adsorbed hydrogen takes advantage of the cluster vacancy to bind to the central Pd atom and leaves its adsorption site as dihydrogen upon the entry of a second H atom. In agreement with the experiment, the encapsulated hydride located opposite the cluster vacancy was found not to directly participate in the HER reaction pathway but rather contributes to maintaining the stability of the cluster and its open structure throughout the HER process. Similar results were observed in cluster **2**. The hydrogen adsorption energy (ΔG_H) on **2**, computed under the conditions of a standard hydrogen electrode at zero overpotential, using the approach proposed by Nørskov *et al*,[49] is 0.93 eV. This value is comparable to that found for $[PdHCu_{11}\{S_2P(O^iPr)_2\}_6(CCPh)_4]$ (1.08 eV) and is consistent with the even better electrocatalytic performance of **2**.

Conclusion

In this study, we present three new Pt-doped Cu-rich hydride clusters co-protected by dithiophosphate and alkynyl ligands (**1**, **2**, and **3**). Cluster **1** can be prepared by several methods, including the direct synthesis from the reduction of a mixture of Cu(I) and Pt(II) salts by sodium borohydride in the presence of dithiophosphates and phenylacetylene. The neutron crystal structure of **1** reveals a bicapped icosahedral copper cage embedding a linear PtH_2 unit. Treatment of **1** with CF_3COOH led to the isolation of **2** and **3**. The structure of **2**, exhibits a *vacancy defect fcc* cuboctahedral $Pt@Cu_{11}$ metallic core. The copper skeleton of **3** can be viewed as a distorted 3,3,4,4,4-pentacapped trigonal prism, also embedding a linear PtH_2 unit. Clusters **1** and **3** can be described as the result of the protonation of 4e-electron oblate NCs, leading to the formation of $[PtH_2]^{2-}@[Cu_{14}]^{14+}$ and $[PtH_2]^{2-}@[Cu_{11}]^{11+}$ host/guest nesting, respectively. On the other hand, cluster **2,** with its incomplete $[PtH@Cu_{11}]^{10+}$ cuboctahedral core, is a 2-electron defective (*nido*-type) superatom. Notably, unlike **1** and **3**, **2** demonstrate exceptional HER electrocatalytic activity, setting a new benchmark for atom precise NCs. It exhibits near-zero onset potential of -0.03 V (at 10 mA cm^{-2}), a Tafel slope of 39 mV dec^{-1} and Faradaic efficiencies exceeding 98 %, and a TOF value of 526 s^{-1} at η= 0.1 V. The structural comparison between the HER-inactive **1, 3** and HER-active **2** NCs provides a new concept into the structural factors that determine the HER activity of Pt-doped Cu-rich hydrides NCs.

Acknowledgements

Acknowledgements Text. This work was supported by the National Science and Technology Council of Taiwan (112-2123-M-259-001), the GENCI computing resource (grant A0090807367), the National Research Foundation of Korea grants (NRF-2022R1A2C3003610 and Carbon-to-X Project No. 2020M3H7A1096388), and Single-crystal neutron diffraction performed on TOPAZ used resources at the Spallation Neutron Source, a DOE Office of Science User Facility operated by the Oak Ridge National Laboratory, under contract no. DE-AC05-00OR22725 with UT-Battelle, LLC.

Conflict of Interest

The authors declare no conflict interest.

Keywords: Copper • hydride • hydrogen evolution reaction • platinum

[1] V. S. Thoi, Y. Sun, C. R. Long, C. J. Chang, *Chem. Soc. Rev.* **2013**, *42*, 2388-2400.

[2] R. M. Bullock, A. M. Appel, M. L. Helmm, *Chem. Commun.* **2014**, *50*, 3125-3143.

[3] Z. Ma, L. Niu, W. Jiang, C. Dong, G. Liu, D. Qu, L. An, Z. Sun, *J. Phys. Mater.* **2021**, *4*, 042002.

[4] J. Zhang, Y. Zhao, X. Guo, C. Chen, C.-L. Dong, R.-S. Liu, C.-P. Han, Y. Li, Y. Gogotsi, G. Wang, *Nat. Catal.* **2018**, *1*, 985-992.

[5] Y.-Y. Ma, C.-X. Wu, X.-J. Feng, H.-Q. Tan, L.-K. Yan, Y. Liu, Z.-H. Kang, E.-B. Wang, Y.-G. Li, *Energy Environ. Sci*. **2017**, *10*, 788-798.

[6] N. Mahmood, Y. Yao, J.-W. Zhang, L. Pan, X. Zhang, J.-J. Zou, *Adv. Sci.* **2018**, *5*, 1700464.

[7] C. Li, J.-B. Baek, *ACS. Omega* **2019**, *5*, 31-40.

[8] J. N. Hansen, H. Prats, K. K. Toudahl, N. M. Secher, K. Chan, J. Kibsgaard, I. Chorkendorff, *ACS energy Lett.* **2021**, *6*, 1175-1180.

[9] N. Dubouis, A. Grimaud, *Chem. Sci*. **2019**, *10*, 9165-9181.

[10] F.-Y. Yu, Z.-L. Lang, L.-Y. Yin, K. Feng, Y.-J. Xia, H.-Q. Tan, H.-T. Zhu, J. Zhong, Z.-H. Kang, Y.-G. Li, *Nat. Comm*. **2020**, *11*, 490.

[11] B. Zhang, H. Zhu, M. L. Zou, X. R. Liu, H. Yang, M. Zhang, W. W. Wu, J. M. Yao, M. L. Du, *J Mater Sci*. **2017**, *52*, 8207–8218.

[12] F. Wang, H. Yu, T. Feng, D. Zhao, J. Piao, J. Lei, *Front. Chem.* **2020**, *8*, 422-431.

[13] A. Balčiūnaitė, R. C. P. Oliveira, M. S. Yilmaz, Ö. Metin, B. Sljukic, D. M. F. Santos, *ECS Trans*. **2018**, *86*, 701-710.

[14] V. R. Stamenkovic, B. S. Mun, M. Arenz, K. J. J. Mayrhofer, C. A. Lucas, G. Wang, P. N. Ross, N. M. Markovic, *Nature Mater*. **2007**, *6*, 241–247.

[15] R. P. B. Silalahi, Y. Jo, J.-H. Liao, T.-H. Chiu, E. Park, W. Choi, H. Liang, S, Kahlal, J.-Y. Saillard, D. Lee, C. W. Liu, *Angew. Chem. Int. Ed*. **2023**, *62*, e202301272.

[16] K. Kwak, W. Choi, Q. Tang, M. Kim, Y. Lee, D.-e. Jian, D. Lee, *Nat. Commun.* **2017**, *8*, 14723.

[17] Y. Tuo, Q. Lu, C. Chen, T. Liu, Y. Pan, Y. Zhou, J. Zhang, *RSC Adv*. **2021**, *11*, 26326-26335.

[18] J. Zhang, H. Yang, B. Martens, Z. Luo, D. Xu, Y. Wang, S. Zou, J. Fang, *Chem. Sci.* **2012**, *3*, 3302–330.

[19] R. Huang, Z. Sun, S. Chen, S. Wu, Z. Shen, X. Wu, J. Zeng, *Chem. Commun*. **2017**, *53*, 6922–6925.

[20] D. Xu, S. Bliznakov, Z. Liu, J. Fang, N. Dimitrov, *Angew. Chem., Int. Ed.* **2020**, *49*, 1282–1285.

[21] J. Wang, J. W. Chen, J. D. Chen, H. Zhu, M. Zhang, M. L. Du, *Adv. Mater. Interfaces* **2017**, *4*, 1700005.

[22] B. H. Lipshutz, C.-T. Lee, J. M. Servesko, *Org. Lett*. **2007**, *9*, 4713-4716.

[23] S. Rendler, M. Oestreich, *Angew. Chem. Int. Ed*. **2007**, *46*, 498-504.

[24] C. Li, R. Y. Liu, L. T. Jesikiewicz, Y. Yang, P. Liu, S. L. Buchwald, *J. Am. Chem. Soc*. **2019**, *141*, 5062-5070.

[25] G. Dong, Z. Pan, B. Han, Y. Tao, X. Chen, G.-G. Luo, P. Sun, C. Sun, D. Sun, *Angew. Chem. Int. Ed*. **2023**, *62,* e202302595.

[26] G.-G. Luo, Z.-H. Pan, B.-L. Han, G.-L. Dong, C.-L. Deng, M. Azam, Y.-W. Tao, J. He, C.-F. Sun, D. Sun, *Angew. Chem. Int. Ed*. **2023**, *62*, e202306849.

[27] C. W. Liu, B. Sarkar, Y.-J. Huang, P.-K. Liao, J.-C. Wang, J.-Y. Saillar, S. Kahlal, *J. Am. Chem. Soc*. **2009**, *131*, 11222-11233.

[28] P.-K. Liao, B. Sarkar, H.-W. Chang, J.-C. Wang, C. W. Liu, *Inorg. Chem.* **2009**, *48*, 4089-4097.

[29] P.-K. Liao, K.-G. Liu, C.-S. Fang, C. W. Liu, J. P. Frackler, Jr., Y.-Y. Wu, *Inorg. Chem*. **2011**, *50*, 8410-8417.

[30] P.-K. Liao, C.-S. Fang, A. J. Edwards, S. Kahlal, J.-Y. Saillar, C. W. Liu, *Inorg. Chem*. **2012**, *51*, 6577-6591.

[31] R. S. Dhayal, J.-H. Liao, X. Wang, Y.-C. Liu, M.-H. Chiang, S. Kahlal, J.-Y. Saillard, C. W. Liu, *Angew. Chem. Int. Ed*. **2015**, *54*, 13604-13608.

[32] A. J. Edwards, R. S. Dhayal, P.-K. Liao, J.-H, Liao, M.-H. Chiang, R. O. Piltz, S. Kahlal, J.-Y. Saillard, C. W. Liu, *Angew. Chem. Int. Ed*. **2014**, *53*, 7214-7218.

[33] R. P. B. Silalahi, J.-H. Liao, Y.-F. Tseng, T.-H. Chiu, S. Kahlal, J.-Y. Saillard, C. W. Liu, *Dalton Trans*. **2023**, *52*, 2106-2114.

[34] S. K. Barik, S.-C. Huo, C.-Y. Wu, T.-H. Chiu, J.-H. Liao, X. Wang, S. Kahlal, J.-Y. Saillard, C. W. Liu, *Chem. Eur. J.* **2020**, *26*, 10471-10479.

[35] R. S. Dhayal, J.-H. Liao, S. Kahlal, X. Wang, Y.-C. Liu, M.-H. Chiang, W. E. van Zyl, J.-Y. Saillard, C W. Liu, *Chem. Eur. J.* **2015**, *21*, 8369-8374.

[36] R. S. Dhayal, W. E. van Zyl, C. W. Liu, *Acc. Chem. Res*. **2016**, *49*, 1, 86–95.

[37] K. K. Chakrahari, J. Liao, R. P. B. Silalahi, T.-H. Chiu, J.-H. Liao, X. Wang, S. Kahlal, J.-Y. Saillard, C. W. Liu, *Small* **2021**, *17*, 2002544.

[38] K. K. Chakrahari, R. P. B. Silalahi, T.-H. Chiu, X. Wang, N. Azrou, S. Kahlal, Y.-C. Liu, M.-H. Chiang, J.-Y. Saillard, C. W. Liu, *Angew. Chem. Int. Ed*. **2019**, *58*, 4943-4947.

[39] R. P. B. Silalahi, Q. Wang, J.-H. Liao, T.-H. Chiu, Y.-Y. Wu, X. Wang, S. Kahlal, J.-Y. Saillard, C. W. Liu, *Angew. Chem. Int. Ed.* **2022**, *61*, e202113266.

[40] S. Lee, M. S. Bootharaju, G. Deng, S. Malola, H. Häkkinen, N. Zheng, T. Hyeon. *J. Am. Chem. Soc*. **2021**, *143*, 12100-12107.

[41] M. Gianini, W. R. Caseri, V. Gramlich, U. W. Suter, *Inorg. Chim. Acta.* **2000**, *299*, 199-208.

[42] R. P. B. Silalahi, G.-R. Huang, J.-H. Liao, T.-H. Chiu, K. K. Chakrahari, X. Wang, J. Cartron, S. Kahlal, J.-Y. Saillard, C. W. Liu, *Inorg. Chem.* **2020**, *59*, 2536-2547.

[43] T. G. Appleton, Encyclopedia of spectroscopy and spectrometry, *Academic Press*, **2017**.

[44] R. P. B. Silalahi, T.-H. Chiu, J.-H. Kao, C.-Y. Wu, C.-W. Yin, Y.-C. Liu, Y. J. Cheng, J. -Y. Saillard, M.-H. Chiang, C. W. Liu, *Inorg. Chem.* **2021**, *60*, 10799-10807.

[45] R. P. B. Silalahi, K. K. Chakrahari, J.-H. Liao, S. Kahlal, Y.-C. Liu, M.-H. Chiang, J.-Y. Saillard, C. W. Liu, *Chem. Asian J.* **2018**, *13*, 500-504.

[46] K. K. Chakrahari, J.-H. Liao, S. Kahlal, Y.-C. Liu, M.-H. Chiang, J.-Y. Saillard, C. W. Liu, *Angew. Chem. Int. Ed.* **2016**, *55*, 14704-14708.

[47] C. Latouche, S. Kahlal, Y.-R. Lin, J.-H. Liao, E. Furet, C. W. Liu, J.-Y. Saillard, *Inorg. Chem*. **2013**, *52*, 13253-13262.

[48] T. Shinagawa, A. T. Garcia-Esparza K. Takanabe, *Sci. Rep*. **2015**, *5*, 1380.

[59] J. K. Nørskov, T. Bligaard, A. Logadottir, J. R. Kitchin, J. G. Chen, S. Pandelov, U. Stimming, *J. Electrochem. Soc.* **2005**, *152*, J23-J26.

[50] Deposition numbers (https://www.ccdc.cam.ac.uk/services/structures?id=doi:10.1002/chem.202303755) 2296486 (for **1**), 2296487 (for $\mathbf{1_N}$), 2296488 (for **2**), and 2296489 (for **3**) contain the supplementary crystallographic data for this paper. These data are provided free of charge by the joint Cambridge Crystallographic Data Centre and Fachinformationszentrum Karlsruhe Access Structure (http://www.ccdc.cam.ac.uk/structures) service.

Entry for the Table of Contents

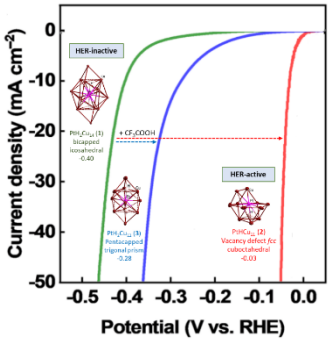

To optimize the HER performance, the size, composition, and structure of bimetallic PtH-Cu NCs are controlled with atomic precision. The addition of CF_3COOH to cluster **1** resulted in the structural change from a bicapped icosahedral Cu_{14} cage encapsulating a linear PtH_2 unit (HER-inactive cluster) to a vertex-missing Cu_{11} cuboctahedron encaging a PtH moiety in cluster **2** (HER-active cluster) and distorted 3,3,4,4,4-pentacapped trigonal prismatic Cu_{11} cage enclosing a PtH_2 unit in cluster **3**. Cluster **2** reveals the highest HER activity among the bimetallic NC catalysts with a near-zero onset potential (η) of -0.03 V (at 10 mA cm^{-2}).